Numerical Analysis on Separation Dynamics of Strap-On Boosters in the Dense Atmosphere

Seongjin Choi*, Soon-Heum Ko, Chongam Kim*** and Oh-Hyun Rho*****
Department of Aerospace Engineering, Seoul National University
Seoul, 151-742, Korea

Jeong-joo Park****
Korea Aerospace Research Institute, Yusung, 305-606, Korea

Abstract

A numerical technique for simulating the separation dynamics of strap-on boosters jettisoned in the dense atmosphere is presented. Six degree of freedom rigid body equations of motion are integrated into the three-dimensional unsteady Navier-Stokes solution procedure to determine the dynamic motions of strap-ons. An automated Chimera overlaid grid technique is introduced to achieve maximum efficiency for multi-body dynamic motion and a domain division technique is implemented in order to reduce the computational cost required to find interpolation points in the Chimera grids. The flow solver is validated by comparing the computed results around the Titan Ⅳ launch vehicle with experimental data. The complete analysis process is then applied to the H-Ⅱ launch vehicle, the central rocket in Japans space program, the CZ-3C launch vehicle developed in China and the KSR-Ⅲ, a three-stage sounding rocket being developed in Korea. From the analyses, separation trajectories of strap-on boosters are predicted and aerodynamic characteristics around the vehicles at every time interval are examined. In addition, separation-impulse devices generally introduced for safe separation of strap-ons are properly modeled in the present paper and the jettisoning force requirements are examined quantitatively.

Key Word : Chimera Overlaid Grid , Separation Dynamics , Rigid Body Equations of Motion

Nomenclature

$\hat{Q}$	conservative variable vector	$\hat{E}, \hat{F}, \hat{G}$	flux vectors
c	speed of sound	p	pressure
γ	specific heat ratio	ρ	density
$\overline{F}$	resultant force vector	Fx, Fy, Fz	x-, y- and z- component of $\overline{F}$
$\overline{h}$	angular momentum vector	hx, hy, hz	x-, y- and z- component of $\overline{h}$
$\overline{M}$	resultant moment vector about mass center	Mx, My, Mz	x-, y- and z- component of $\overline{M}$
		Iij	moment of inertia
$\overline{\tau}$	shear stress vector	$\overline{\omega}$	angular velocity vector
$\overline{v}$	velocity vector	$d\alpha$	angular displacement vector
ds	displacement vector		

* Ph.D Candidate in Aerodynamic Simulations Lab
** M.S. Candidate in Aerodynamic Simulations Lab
*** Professor, Seoul National University
E-mail : chongam@plaza.snu.ac.kr, TEL : 02-880-1915, FAX : 02-887-2662
**** Head of the Rocket System Development Team

Introduction

The accurate simulation of separated bodies in the dense atmosphere has been of great interest for several years. One major area of application for this technology lies in the separation dynamics of boosters from the parent. The strap-on boosters have been used to increase the payload capabilities of rockets and for the safe separation of boosters without catastrophic collision, the separation dynamics of the spent strap-on bodies from the parent rocket should be analyzed in detail with a desired accuracy. Many researchers have investigated this field numerically or experimentally. Meakin[1] of NASA Ames analyzed the SRB (Solid Rocket Booster) separation of a space shuttle with a Navier-Stokes solver. In his research, however, a prescribed trajectory was used for the dynamic analysis of body motion. Lochan and Adimurthy[2] attempted to analyze the separation dynamics of strap-on boosters from the core rocket but they used wind tunnel simulation data for the measurement of aerodynamic forces. And Lijewski[3] developed an unsteady simulation technique for store separation from a delta wing. In addition, with regard to vehicles with strap-on boosters, Palmer[4] analyzed the flow field around the Conestoga 1620 launch vehicle with six boosters. Similar analyses were carried out by Taylor[5] and Azevedo[6] for the Titan Ⅳ with two boosters, AVLS launch vehicle with four boosters, respectively. Their studies were, however, focused on steady state aerodynamic analyses without considering the relative motion of boosters. In fact, only a few numerical investigations seem to be reported, especially for the aerodynamic-dynamic coupled analysis for the separation of strap-ons, although multi-stage launch vehicles with boosters are widely used for many years.

Thus the present paper focused on developing an efficient aerodynamic-dynamic coupled numerical solver to simulate booster separation dynamics of multi-stage vehicles. Six degree of freedom rigid body equations of motion are integrated into the three-dimensional unsteady Navier-Stokes solver. And an automated Chimera overlaid grid technique is introduced to achieve maximum efficiency for multi-body dynamic motion and a domain division technique is implemented in order to reduce the computational cost required to find interpolation points in the Chimera grids. The developed flow solver is validated by comparing the computed results around the Titan Ⅳ launch vehicle with experimental data. The complete analysis process is then applied to three vehicle models of H-Ⅱ, CZ-3C and KSR-Ⅲ. H-Ⅱ is a two stage rocket with two solid strap-ons, which has been the central rocket in Japanese space program. CZ-3C was developed in China, which had two strap-ons, too. KSR-Ⅲ is a three stage sounding rocket with two large strap-ons, which is now being developed in Korea. The detailed geometry of these vehicles are described in the following section of this paper. From these analyses, trajectories of strap-on boosters during separation stages are predicted and aerodynamic characteristics around the vehicles are examined. For safe separation of boosters, some additional jettisoning forces and moments are generally introduced by using separation-impulse devices such as spring ejectors or retro rockets. In this paper these separation-impulse devices are properly modeled and the guideline map of additional jettisoning force and moment for safe separation is presented.

Description of Vehicles

The H-Ⅱ, the CZ-3C and the KSR-Ⅲ investigated in the present paper have symmetric configurations with two strap-on boosters and the details of the geometry are shown in Fig 1. In the configuration of H-Ⅱ the strap-on boosters are much smaller than the core rocket in diameter and length. CZ-3C has similar configuration, but it has a core rocket of singular shape. However, the strap-ons of KSR-Ⅲ are about the same size as the core in order to employ the same rocket engine in both components. Thus the detailed analysis of the interactions between the core rocket and boosters during separation stages may be particularly important in KSR-Ⅲ. The nozzles of the rockets are not considered in actual simulation assuming that their effects on the separation dynamics

is not critical. Specifications of the weight of bodies, the positions of center of gravity and separation-impulse devices for three vehicles are presented in Table 1. The core rocket has two connectors for each booster and the boosters are separated by the aerodynamic forces, gravity and additional jettisoning forces as shown in Fig 2.

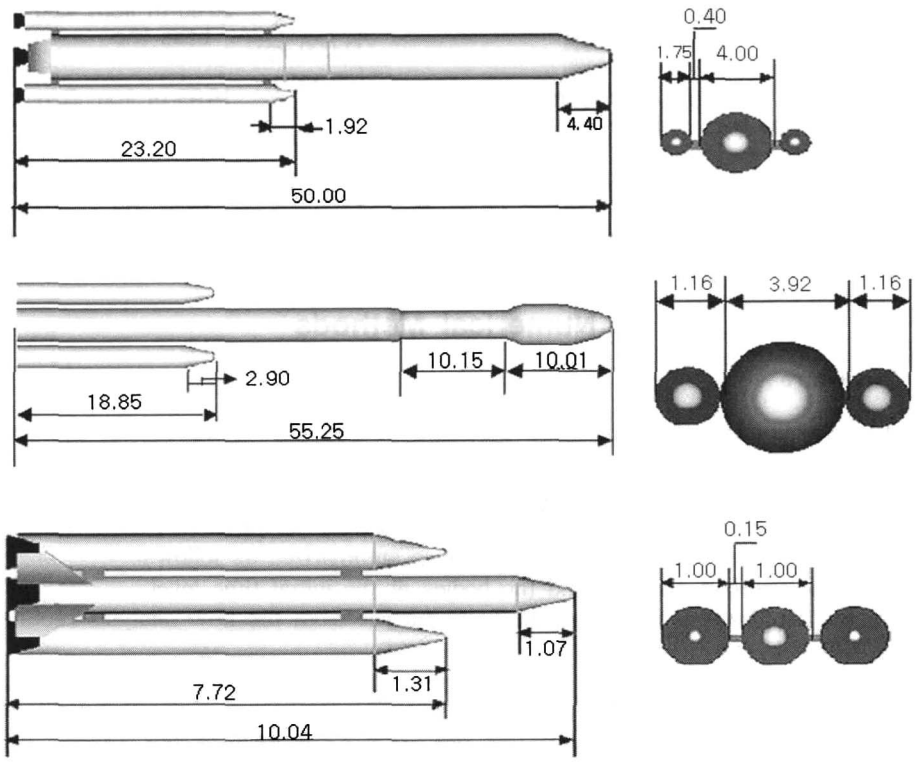

Fig. 1. Configurations of Rockets
a) H-II b) CZ-3C c) KSR-III

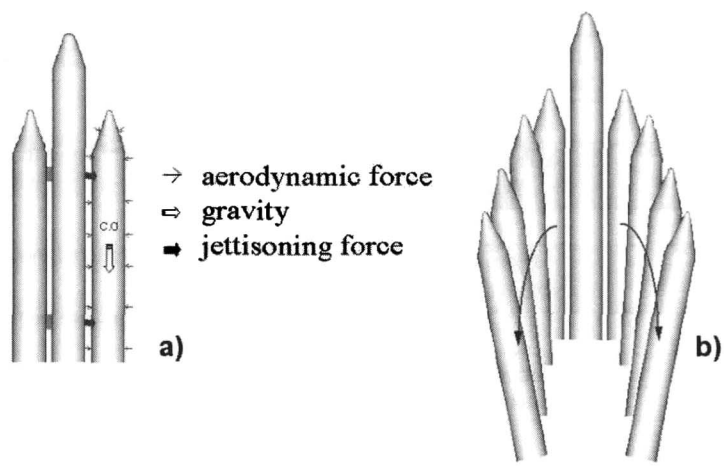

Fig. 2. Separation Motion of Boosters
a) Forces Acting on Boosters b) Booster Trajectory

Table 1. Core Rocket and Booster Characteristics

	C.G. of Core Rocket	C.G. of Booster	Weight of Core Rocket	Weight of Booster	Location of Ejector 1	Location of Ejector 2
H - II	20.60 m from base line	10.88 m from base line	120,000 kg	70,000 kg (fuel free : 11,000 kg)	20.80 m from base line	4.00 m from base line
CZ - 3C	26.05 m from base line	8.41 m from base line	239,150 kg	179,000 kg (fuel free : 9,000 kg)	15.95 m from base line	5.51 m from base line
KSR - III	4.66 m from base line	3.42 m from base line	5,500 kg	4,600 kg (fuel free : 1,000 kg)	5.80 m from base line	1.00 m from base line

Numerical Methods

Solution Procedure

In order to simulate the separation dynamics of bodies in compressible flow regime, it is necessary to understand the transient flowfields on and around the bodies. The obtained aerodynamic forces including gravity effect cause the relative motion of boosters. That is, the trajectory of boosters is predicted by the solutions of six-DOF (degree of freedom) equations of motion with aerodynamic forces from a flow solver. The solution procedure is summarized as follows:

a. Generate the overlaid grids around the bodies at the initial time level.

b. Obtain the aerodynamic forces on the body surface from the flow analysis routine at initial time.

c. Convert the aerodynamic forces including gravity and other additional control forces into the force and moment components acting on the C.G (center of gravity) of the body.

d. Solve the rigid body equations of motion and get the new position and velocity components of the body at a next time level.

e. Move the body grids and interpolate flow information at fringe cells.

f. Repeat the unsteady analysis routine of b ~ e

This solution procedure is illustrated in Fig. 3.

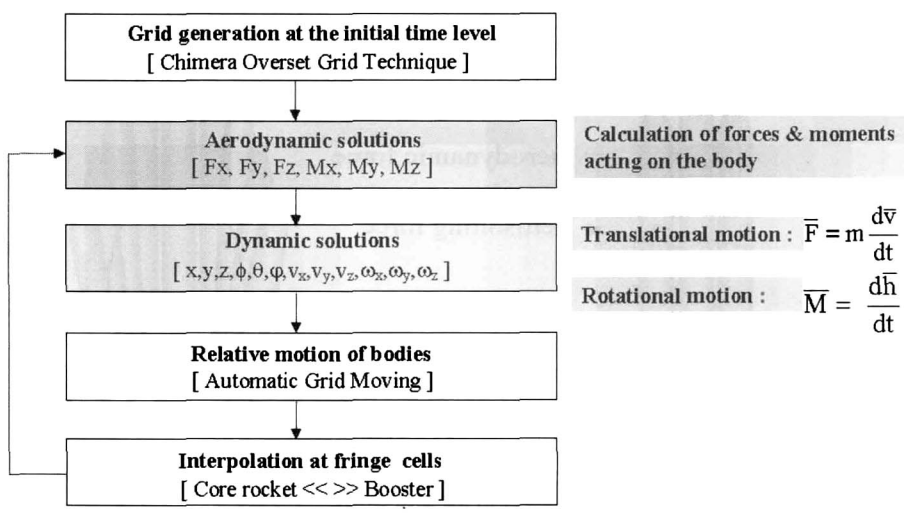

Fig. 3. Solution procedure

Flow Analysis

Since the present vehicles does not contain massive flow separation regions except for the base flow region whose effects are not considered in the present research, the three-dimensional compressible thin-layer Navier-Stokes Equations are adopted for an efficient flow analysis. The thin-layer Navier-Stokes equations can be written in general curvilinear coordinates ξ, η, ζ as follows:

$$\frac{\partial \hat{Q}}{\partial t}+\frac{\partial \hat{E}}{\partial \xi}+\frac{\partial \hat{F}}{\partial \eta}+\frac{\partial \hat{G}}{\partial \zeta}=\frac{1}{Re}\frac{\partial \hat{G}_v}{\partial \zeta} \tag{1}$$

where

$$\hat{Q}=\frac{1}{J}\begin{pmatrix}\rho\\ \rho u\\ \rho v\\ \rho w\\ e\end{pmatrix},\ \hat{E}=\frac{1}{J}\begin{pmatrix}\rho U\\ \rho uU+\xi_x p\\ \rho vU+\xi_y p\\ \rho wU+\xi_z p\\ (e+p)U-\xi_t p\end{pmatrix},\ \hat{F}=\frac{1}{J}\begin{pmatrix}\rho V\\ \rho uV+\eta_x p\\ \rho vV+\eta_y p\\ \rho wV+\eta_z p\\ (e+p)V-\eta_t p\end{pmatrix},\ \hat{G}=\frac{1}{J}\begin{pmatrix}\rho W\\ \rho uW+\zeta_x p\\ \rho vW+\zeta_y p\\ \rho wW+\zeta_z p\\ (e+p)W-\zeta_t p\end{pmatrix},$$

$$\hat{G}_v=\frac{1}{J}\begin{pmatrix}0\\ m_1u_\zeta+m_2\zeta_x\\ m_1v_\zeta+m_2\zeta_y\\ m_1w_\zeta+m_2\zeta_z\\ m_1m_3+\frac{m_2}{3}(\zeta_x u+\zeta_y v+\zeta_z w)\end{pmatrix}\quad with\quad \begin{aligned} m_1&=\mu(\zeta_x^2+\zeta_y^2+\zeta_z^2)\\ m_2&=\mu(\zeta_x u_\zeta+\zeta_y v_\zeta+\zeta_z w_\zeta)\\ m_3&=\frac{\mu}{2}(u^2+v^2+w^2)_\zeta+\frac{\mu}{\Pr}\frac{(c^2)_\zeta}{\gamma-1}\end{aligned}$$

and U, V, W are contravariant velocity components which can be written as

$$U=\xi_x u+\xi_y v+\xi_z w\ ,\quad V=\eta_x u+\eta_y v+\eta_z w\ ,\quad W=\zeta_x u+\zeta_y v+\zeta_z w$$

In Eq.(1), the viscous terms involving velocity gradients in the axial direction ξ, the radial direction η are neglected and velocity gradients in the normal direction ζ are collected into the vector $\hat{G}_v$. Turbulent viscous components are evaluated using the Baldwin-Lomax algebraic turbulence model[7] with a modified Degani-schiff technique.[8]

For the temporal discretization of unsteady flowfield, dual time stepping is employed to obtain a second order accuracy.

$$\frac{\partial \hat{Q}}{\partial \tau}=-\hat{R}^{n+1,s+1}-\frac{3\hat{Q}^{n+1,s+1}-4\hat{Q}^n+\hat{Q}^{n-1}}{2\Delta t} \tag{2}$$

where $\hat{R}=\frac{\partial \hat{E}}{\partial \xi}+\frac{\partial \hat{F}}{\partial \eta}+\frac{\partial(\hat{G}-\hat{G}_v)}{\partial \zeta}$. Here τ represents a pseudo time, n is the physical time level, and s is the pseudo time level. Equation (2) is discretized in pseudo time by the Euler implicit method and is linearized using the flux Jacobian. This leads to a large system of linear equations in delta form at each pseudo time step as

$$\left[\frac{I}{J\Delta\tau}+\left(\frac{\partial R}{\partial Q}\right)+\frac{1.5I}{J\Delta t}\right]\Delta Q=-R^{n+1,s}-\frac{3Q^{n+1,s}-4Q^n+Q^{n-1}}{2J\Delta t} \tag{3}$$

As the implicit time integration method of equation (3) LU-SGS (Lower-Upper Symmetric Gauss-Seidel) scheme[9] is used. The viscous flux Jacobian is neglected in the implicit part since it does not influence a solution accuracy, and local time stepping is used.

As a spatial discretization, AUSMPW+(modified Advection Upstream Splitting Method Press-based Weight function)[10] has been applied. It was designed to remove the non-monotone pressure solutions of the hybrid flux splitting schemes such as AUSM and AUSM+ by introducing pressure weighting functions as a limiter at a cell interface. In AUSMPW+ the flux vector at a cell interface can be represented as follows;

$$\hat{F}_{\frac{1}{2}} = \overline{M}_L^{+} c_{\frac{1}{2}} \boldsymbol{\Phi}_L + \overline{M}_R^{-} c_{\frac{1}{2}} \boldsymbol{\Phi}_R + (P_L^{+} \boldsymbol{P}_L + P_R^{-} \boldsymbol{P}_R) \tag{4}$$

$\overline{m}^{+}$ and $\overline{m}^{-}$ changes as the sign of Mach number at the cell interface.

i) $M_{\frac{1}{2}} \geq 0$

$$\overline{M}_L^{+} = M_L^{+} + M_R^{-} \times ((1-w)\cdot(1+f_R) - f_L) ,$$
$$\overline{M}_R^{-} = m_R^{-} \times w(1+f_R)$$

ii) $M_{\frac{1}{2}} < 0$

$$\overline{M}_L^{+} = m_L^{+} \times w(1+f_L) ,$$
$$\overline{M}_R^{-} = M_R^{-} + M_L^{+} \times ((1-w)\cdot(1+f_L) - f_R)$$

where

$$\boldsymbol{\Phi}_{L,R} = (\rho \ \rho u \ \rho v \ \rho w \ \rho H)^T , \quad \boldsymbol{P}_{L,R} = (0 \ \overline{n}_x p_{L,R} \ \overline{n}_y p_{L,R} \ \overline{n}_z p_{L,R} \ 0)^T$$

$$w(p_L, p_R) = 1 - \min\left(\frac{p_L}{p_R}, \frac{p_R}{p_L}\right)^3$$

and function f is simplified as follows:

$$f_{L,R} = \begin{cases} \dfrac{p_{L,R}}{p_s} - 1 , & |M_{L,R}| < 1 , \ p_s \neq 0 \\ 0 , & elsewhere \end{cases}$$

where $p_s = \boldsymbol{P}_L^{+} p_L + \boldsymbol{P}_R^{-} p_R$. The split Mach number and the split pressure of AUSMPW+ at a cell-interface are also simplified as follows:

$$M^{\pm} = \pm \frac{(M \pm 1)^2}{4} , \qquad |M| < 1$$
$$= \frac{1}{2}(M \pm |M|) , \qquad |M| \geq 1$$

$$P^{\pm} = \frac{(M \pm 1)^2}{4}(2 \mp M) , \qquad |M| < 1$$
$$= \frac{1}{2}(1 \pm sgn(M)) , \qquad |M| \geq 1$$

And $M_{L,R} = \dfrac{U_{L,R}}{c_{\frac{1}{2}}}$, where $c_{\frac{1}{2}}$ is the speed of sound at a cell interface.

For a higher-order spatial accuracy, MUSCL(Monotone Upstream-centered Schemes for Conservation Laws)[11] approach is used. Primitive variables are extrapolated at a cell interface, and the differentiable limiter[12] is employed to suppress unphysical oscillations near physical discontinuities.

Dynamic Analysis

The reference frames of the multi-stage rocket system are shown in Fig.4. XYZ frame is fixed at the C.G. of core rocket and xyz frame is at the C.G. of booster. At the initial stage, the corresponding axes at two frames point to the same direction. At the moving stage, XYZ frame is fixed at the space and xyz frame makes a relative motion to the XYZ frame as booster separates from the core rocket, changing the direction of axes. To know the movement and rotation of booster body, six degree of freedom rigid body equations of motion must be solved.

The basic equations of rigid body motion with respect to the coordinates XYZ attached to the core rocket is expressed as

$$\overline{F}_{cg}=(m\frac{d\overline{v}}{dt})_{XYZ}\ ;\quad \overline{M}_{cg}=(\frac{d\overline{h}}{dt})_{XYZ} \tag{5}$$

In these equations $\overline{F}_{cg}$, $\overline{M}_{cg}$ are external force and moment vector acting on the C.G of the body and they are represented as follows;

$$\begin{aligned}\overline{F}_{cg} &= \overline{F}_{ad}+\overline{F}_{gv}+\overline{F}_{ct}\\ \overline{M}_{cg} &= \overline{r}_0\times(\overline{F}_{ad}+\overline{F}_{gv}+\overline{F}_{ct})\end{aligned} \tag{6}$$

Here, $\overline{F}_{gv}$, $\overline{F}_{ct}$ represent gravity and additional control forces and the aerodynamic forces,

$$\overline{F}_{ad}=\int_s(-p\hat{n}+\overline{\tau})dS \tag{7}$$

In Eq.(5) $\overline{v}$, $\overline{h}$ are velocity and angular momentum vector with respect to center of mass of the body and the angular momentum, $\overline{h}(h_X, h_Y, h_Z)$ is expressed as

$$\begin{aligned}h_X &= \omega_X I_{XX}-\omega_Y I_{XY}-\omega_Z I_{XZ}\\ h_Y &= -\omega_X I_{XY}+\omega_Y I_{YY}-\omega_Z I_{ZY}\\ h_Z &= -\omega_X I_{XZ}-\omega_Y I_{ZY}+\omega_Z I_{ZZ}\end{aligned} \tag{8}$$

Since the moments and products of inertia of the body would change continually due to its rotation, it is necessary to determine their values as functions of time. It is, therefore, more convenient to use the coordinates xyz attached to the rotating booster as shown in Fig. 4, which ensures that its moments and products of inertia maintain the same values during the motion. Then, the moment equations relative to the moving coordinate system xyz with an angular velocity $\overline{\omega}$, become

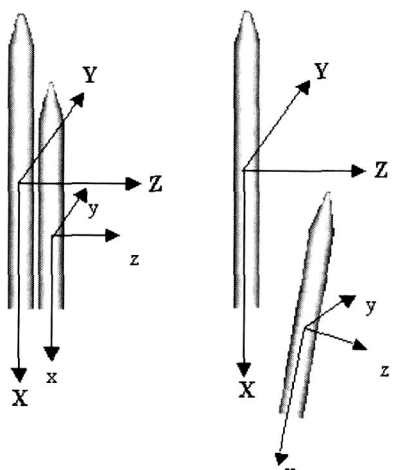

XYZ : axes of fixed orientation

xyz : body fixed axes

Fig. 4. Reference frames

$$\overline{M}_{cg}=(\frac{d\overline{h}}{dt})_{xyz}+\overline{\omega}\times\overline{h} \tag{9}$$

Since the xyz axes coincide with the principal axes of inertia of the rotating body, the angular momentum, $\overline{h}$ can be simplified as

$$h_x=\omega_x I_{xx}\ ,\ h_{yy}=\omega_y I_{yy}\ ,\ h_z=\omega_z I_{zz} \tag{10}$$

Then the moment equations of motion are expressed as

$$\begin{aligned}M_x &= I_{xx}\dot{\omega}_x-(I_{yy}-I_{zz})\omega_y\omega_z\\ M_y &= I_{yy}\dot{\omega}_y-(I_{zz}-I_{xx})\omega_z\omega_x\\ M_z &= I_{zz}\dot{\omega}_z-(I_{xx}-I_{yy})\omega_x\omega_y\end{aligned} \tag{11}$$

which are usually referred to as the Euler's equations of motion. With the force relation of Eq.(5) in scalar form,

$$F_x = m\,\dot{v}_x$$
$$F_y = m\,\dot{v}_y \tag{12}$$
$$F_z = m\,\dot{v}_z$$

Eqs.(11) and (12) form a system of six differential equations and have a unique solution if initial conditions are given.

For the calculation of the equations of motion, the force equations are discretized in the inertial coordinate system (XYZ) directly while moment equations are solved in the moving coordinate system (xyz). After computing the aerodynamic forces, moments, and gravity, the new velocity $\bar{v}^{n+1}$ and displacement ds^{n+1} are obtained by

$$\frac{\bar{v}^{n+1} - \bar{v}^{n}}{\Delta t} = \frac{1}{m}\bar{F}^{n}\ ,\quad ds^{n+1} = \frac{1}{2}(\bar{v}^{n} + \bar{v}^{n+1})\Delta t \tag{13}$$

And the new angular momentum $\bar{\omega}^{n+1}$ is calculated from Eq.(11) as

$$\frac{\omega_x^{n+1} - \omega_x^{n}}{\Delta t} = \frac{1}{I_{xx}}[M_x + (I_{yy} - I_{zz})\omega_y\omega_z]$$
$$\frac{\omega_y^{n+1} - \omega_y^{n}}{\Delta t} = \frac{1}{I_{yy}}[M_y + (I_{zz} - I_{xx})\omega_z\omega_x] \tag{14}$$
$$\frac{\omega_z^{n+1} - \omega_z^{n}}{\Delta t} = \frac{1}{I_{zz}}[M_z + (I_{xx} - I_{yy})\omega_x\omega_y]$$

Finally the angular displacement is updated as,

$$da^{n+1} = \frac{1}{2}(\bar{\omega}^{n} + \bar{\omega}^{n+1})\Delta t \tag{15}$$

From above dynamic analysis, the new position and velocity components at a next time level are determined.

Grid Scheme

With moving body problems it is essential to have the initial grid distribution strictly adjusted to the motion of bodies. In this regard unstructured grid technique and overlaid grid technique are known to be the most pertinent ones. Although unstructured grid technique has a good flexibility in generating grids around complex geometry, all grids close to bodies should be carefully regenerated for motion of bodies to maintain the quality of initial grids. Chimera overlaid grid technique can maintain high grid quality only by rotating or translating initial grids in those moving problems. Thus the Chimera overlaid grid technique proposed by Steger[13] is adopted in the present paper. For the efficient communication of conservative variables on the overlaid regions, the tri-linear interpolation technique is introduced and this is based on the Newton-Raphson method in iso-parametric coordinates.

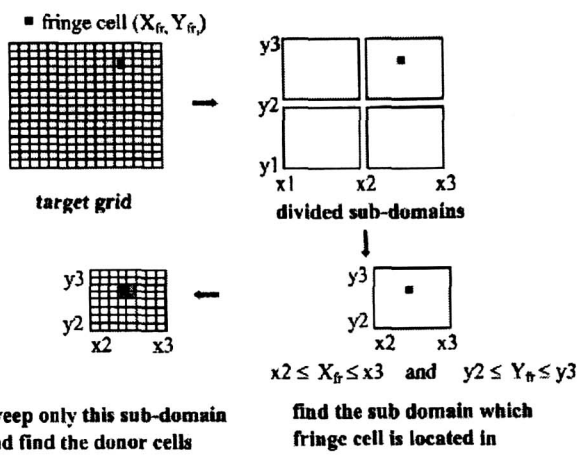

Fig. 5. Domain division technique (two-dimensional case)

The two bodies investigated in the present paper are so close that in both grids the Chimera holes are created respectively. Thus one or more of the 8 donor cells can be in hole region, in that case the nearest cells around the donor in non-hole region are used as substitutes.

In three-dimensional problem it generally takes much time to find the donor cells in the whole grid region. Especially for unsteady problems this searching should be repeated at every time interval and it takes a considerable portion of the whole computational time. In the present paper, a simple domain division technique is introduced to reduce the searching time of nearest cell center of target domain. In this technique the target domain is divided into a number of sub-domains prior to find the nearest cell center. The sub-domain including the fringe cell is then pre-determined by simple comparison of position coordinates. Then fast searching is possible in the determined sub-domain. Figure 5 shows a simple example of domain division technique in two-dimensional case.

The core rocket grid and the booster grid generated independently are shown in Fig. 6-a. One of the moving grids is shown in Fig. 6-b, and the fringe cells of the core rocket grid and booster grid are shown in Fig. 6-c,d.

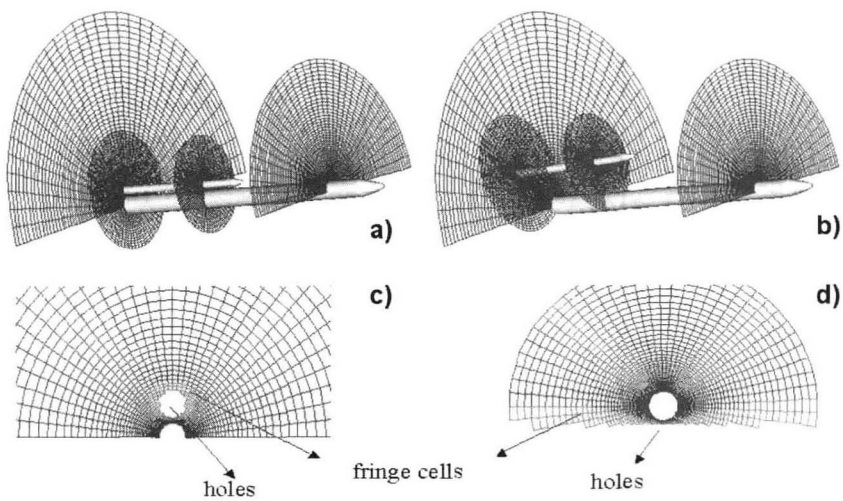

Fig. 6. Grid generation around the core rocket and booster
a) initial stage b) moving stage c) hole & fringe cells in core grid
d) hole & fringe cells in booster grid

Results and Discussion

Flow Solver Validation

As a validation of the developed flow solver which directly influences the trajectory of vehicles, wind tunnel data of the Titan Ⅳ launch vehicle are used.[5] The free stream conditions are the Mach number of 1.6 and the Reynolds number of 1.1×10^7 with zero angle of attack. As shown in Fig. 7, the overlapping grids of $101\times66\times121$ points for the core rocket and $81\times66\times101$ for the booster are used. Figure 8 shows the cross sectional pressure contour of the Titan Ⅳ vehicle and Fig. 9 for the calculated surface pressure along the centerline of the vehicle compared with experimental wind tunnel data. Calculated pressure is non-dimensionalized by $\rho_\infty c_\infty^2$ and x-position denotes the distance from the nose of the core rocket. The close agreement between experimental and computed values can be observed in most regions except for the connecting point of the core rocket and booster where the computed values are a little underestimated due to the effect of a connecting cable in the wind tunnel test.[5]

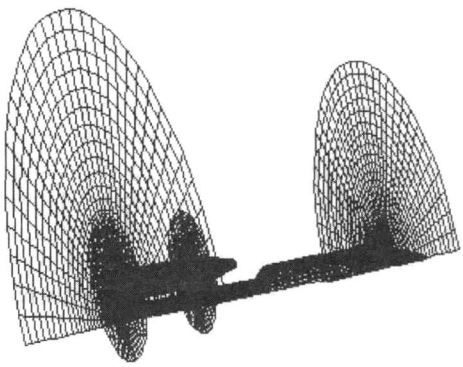

Fig. 7. Grid generation around Titan Ⅳ launch vehicle configuration

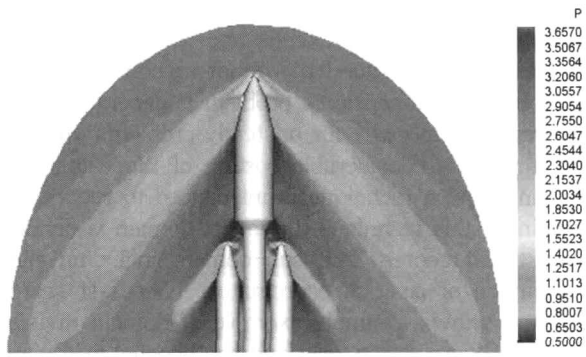

Fig. 8. Pressure contours around Titan Ⅳ launch vehicle (Mach = 1.6, AOA = 0)

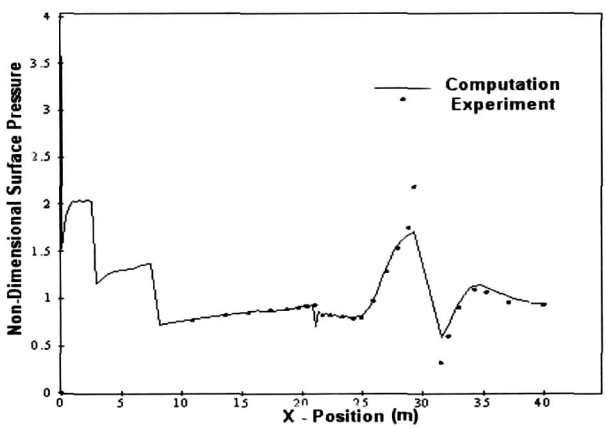

Fig. 9. Comparison of computed surface pressure with wind-tunnel data (along the centerline of the core rocket)

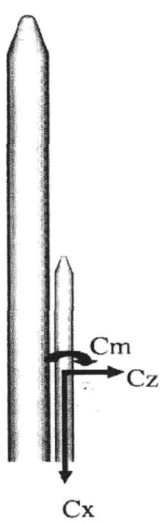

Fig. 10. Directions of Non-dimensional Aerodynamic Forces & Moments

Separation Dynamics of H-Ⅱ

Prior to analyzing the separation dynamics of H-Ⅱ, the aerodynamic characteristics around the bodies at the initial stage of separation are examined and simulations of separation dynamics are presented based on the initial stage results. At the initial stage the free stream Mach number is 2.0 and the Reynolds number is 9.0047×10^6 and $101\times66\times121$ grid points are used for the core rocket and $51\times66\times101$ for the booster. Directions of the non-dimensional axial force Cx, the normal force Cz and the pitching moment Cm are represented in Fig. 10. Non-dimensional forces are calculated by the product of non-dimensional pressure and the area and non-dimensional moment by the product of non-dimensional force and the distance from the center of gravity. As the results, pressure contours on and around the vehicle are shown in Fig. 11 and the non-dimensional forces and moments acting on the surface of the booster

are presented in Table 2. At this initial stage the axial force Cx is surely positive and produces the downward motion of booster with gravity effect. The pitching moment Cm is also positive and makes the positive pitching motion of booster. But the normal force Cz is close to zero, so the distance between the core rocket and booster rarely changes. The convergence behavior of the computed solution is shown in Fig. 12.

Table 2. Non-dimensional Aerodynamic Forces and Moments in the Initial Stage

	Cx	Cz	Cm
H - Ⅱ	0.1161	0.0006	0.0065
CZ - 3C	0.1299	0.0037	-0.0019
KSR - Ⅲ	0.5709	0.0070	-0.0577

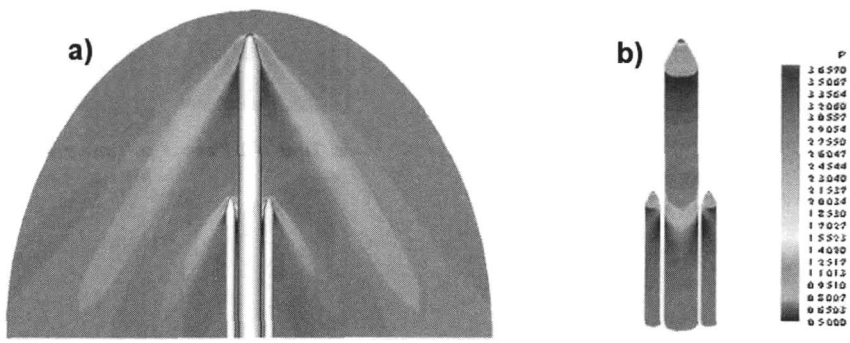

Fig. 11. Pressure Contours of H-Ⅱ at the Initial Stage (Mach = 2.0, Re = 9.0047×10^6)
a) Around the Vehicle b) On the Surface of the Vehicle

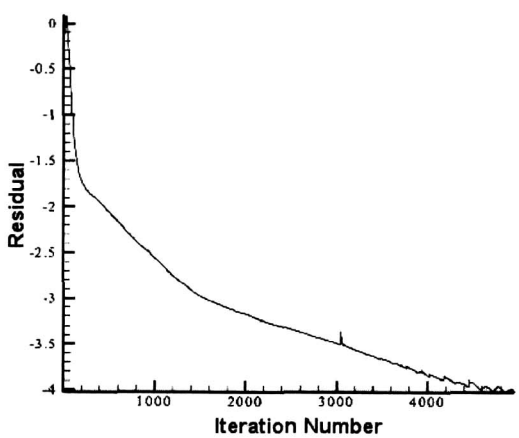

Fig. 12. Convergence History of H-Ⅱ at the Initial Stage (Mach = 2.0, Re = 9.0047×10^6, CFL = 5.0)

Separation dynamics of strap-on boosters is then simulated at the physical time step of 0.005sec. In this simulation the Chimera overlaid moving grid scheme is used with the domain division technique. Firstly, free body separation is simulated where the booster is simply released from the core rocket. From the design of H-Ⅱ, the initial distance between the core rocket and booster is set to 0.4m. As predicted from the initial stage analysis, the booster falls down vertically with a small positive pitching motion as time evolves. In Fig. 13, the trajectory of booster and corresponding pressure contours around the core rocket and booster are shown at every 0.05sec after separation. In this simulation the booster seems to be quite close to the core rocket during all the stages. Thus it would be better to introduce some additional jettisoning forces and moments using separation-impulse devices. The H-Ⅱ uses the spring ejection systems as separation-impulse devices, in the present paper their effects are replaced by the

impact normal forces of different magnitude acting at the two connecting points for initial 0.005 sec. Then a forced separation case is simulated with the non-dimensional jettisoning force of 0.060 and moment of 0.030. Jettisoning force and moment are non-dimensionalized by gravity of booster. Figure 14 shows the booster trajectory and pressure contour around the vehicle in this simulation, and a more safe separation is expected.

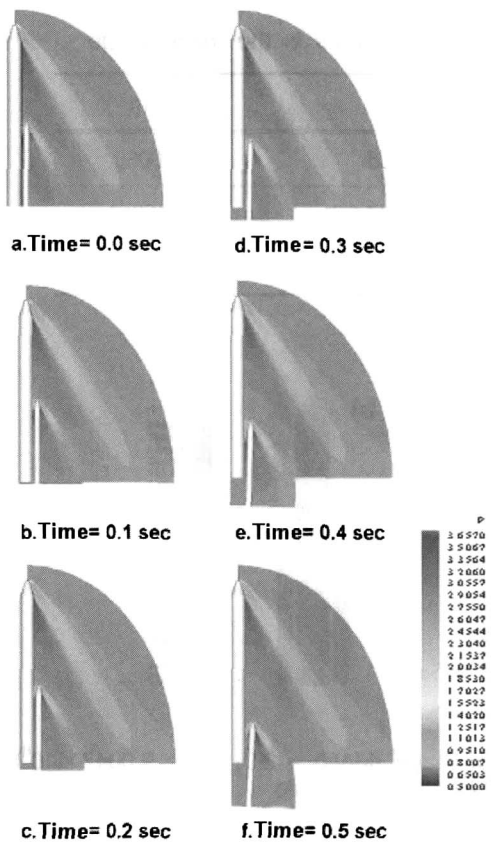

Fig. 13. Booster Trajectory of H-II with Pressure Contours (Free separation, no jettisoning force & moment)

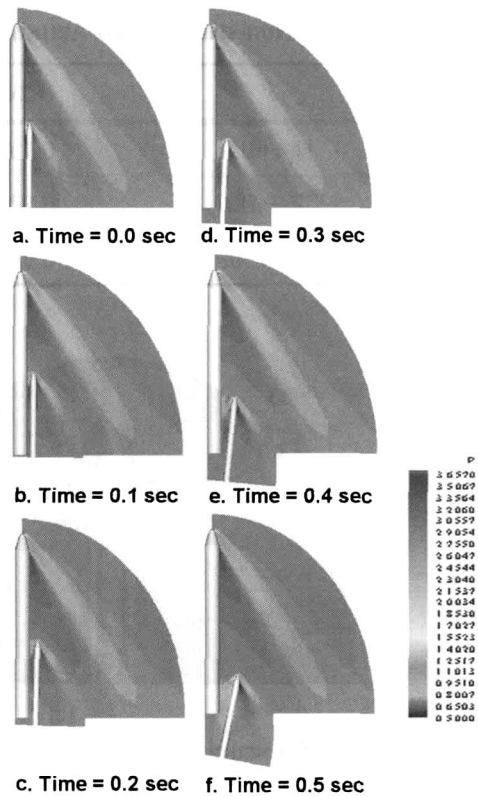

Fig.14. Booster Trajectory of H-II with Pressure Contours (Non-dimensional jettisoning force = 0.060, jettisoning moment = 0.030)

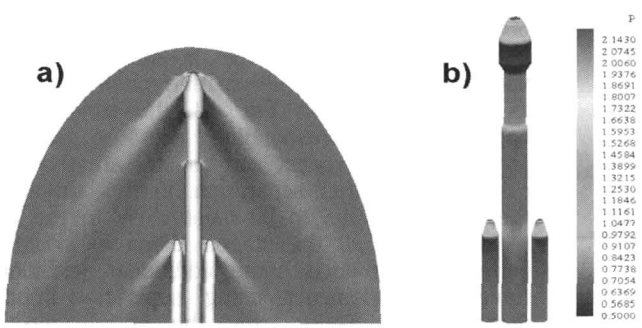

Fig. 15. Pressure Contours of CZ-3C at the Initial Stage (Mach = 2.0, Re = 9.0047×10^6)

Separation Dynamics of CZ-3C

As mentioned earlier, the geometry of CZ-3C is similar to that of H-II. So, firstly we can imagine that the aerodynamic characteristics of CZ-3C is similar to that of H- II. We examine the aerodynamic characteristics of CZ-3C in the same manner. The free stream Mach number is 2.0 and the Reynolds number is 9.0047×10^6, too. $121 \times 66 \times 121$ grid points are used for the core rocket and $81 \times 66 \times 101$ for the booster.

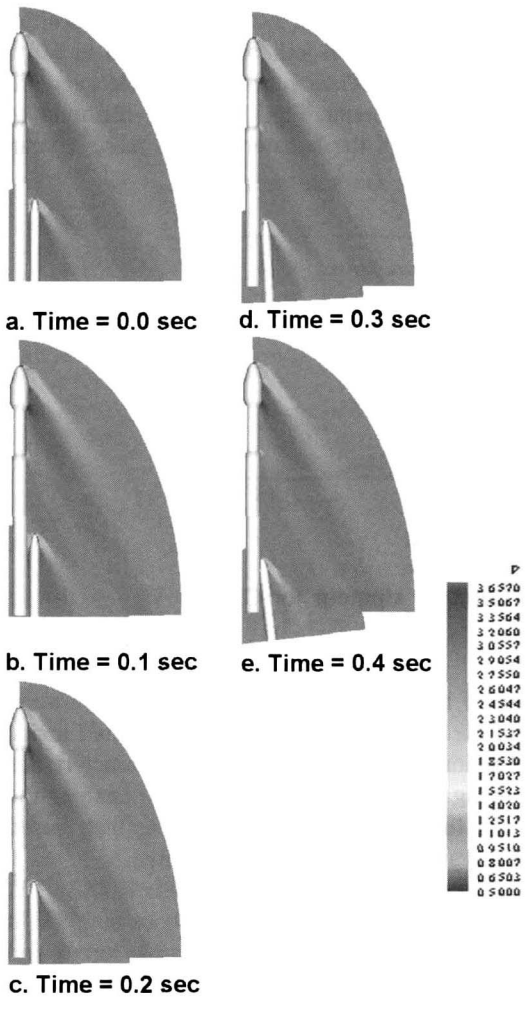

Fig. 16. Booster Trajectory of CZ-3C with Pressure Contours (Free separation, no jettisoning force & moment)

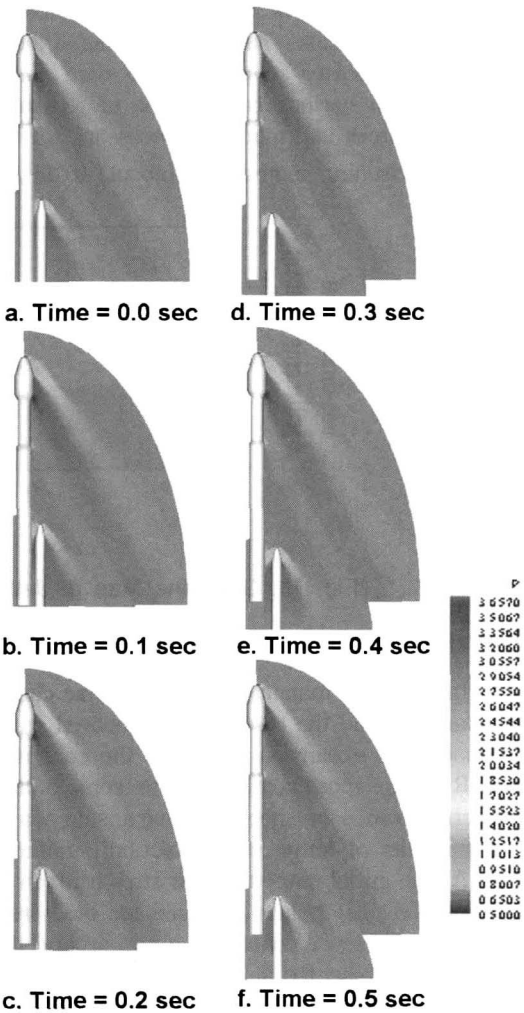

Fig. 17. Booster Trajectory of CZ-3C with Pressure Contours (Non-dimensional jettisoning force = 0.046, jettisoning moment = 0.016)

Pressure contours on and around the vehicle are shown in Fig. 15 and the aerodynamic forces and moments are presented in Table 2. At the initial stage Cx of CZ-3C is nearly the same as that of H-Ⅱ and produces the downward motion of booster with gravity effect. But, comparing the aerodynamic characteristics of CZ-3C with those of H-Ⅱ, Cm has the different manner. In H-Ⅱ, the pitching moment Cm is positive and the nose of booster rotates out of the core rocket at the moving stage. But, in the case of CZ-3C, Cm is negative and booster will rotate to the body of core rocket. Although Cz of CZ-3C is about six times as large as that of H-Ⅱ as shown in Table 2,(It means the C.G. of booster in CZ-3C moves outward from core rocket six times faster than that in H-Ⅱ.) the negative pitching moment acts dominantly, eventually causes booster to collide against core rocket.

Separation dynamics of strap-on boosters in the free separation condition is simulated in Fig.16. Distance between booster and core rocket in initial stage is 0.6m. As time goes on, booster rotates to the counterclockwise direction since Cm is negative. So, the head of the booster goes toward the core rocket and, eventually, booster collides against core rocket during separation (at 0.4sec after separation.). Thus, some additional jettison forces and moments are required to prevent this rocket system from collision.

Figure 17 shows the booster trajectory and pressure contour with other booster separation condition. In this case, the non-dimensional jettisoning force is 0.046 and jettisoning moment is 0.016. In this case, booster separates from core rocket without collision. Then numerous simulations are simulated with various combination of jettisoning forces and moments. Fig. 18 shows the map of jettisoning forces and moments necessary for the safe separation of the booster. In this map, we can see that jettisoning moment of (about) 0.016 is always sufficient for safe separation.

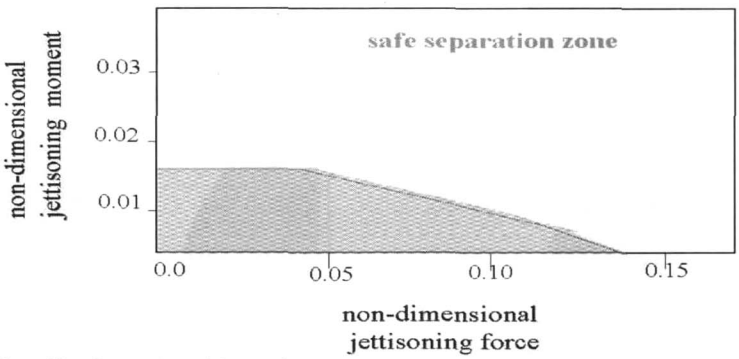

Fig. 18. Guideline Map of Jettisoning Force & Moment for CZ-3C

Separation Dynamics of KSR-Ⅲ

In the same manner the aerodynamic characteristics of KSR-Ⅲ at the initial stage of separation are examined and the results are compared with those of H-Ⅱ. Since the boosters are located inside the shock and expansion waves of the core rocket at the initial stage, the flow field characteristics of KSR-Ⅲ are more complex. Thus some additional investigations are added in order to analyze the interaction trends of shock and expansion waves between the core and booster. And at last, based on the results of initial stage solution, simulations of separation dynamics are presented.

At the initial stage the free stream Mach number is 2.0 and the Reynolds number is 9.0047×10^6. And $101\times66\times121$ points are used for the core rocket grid and $81\times66\times101$ for the booster grid. In Fig. 19, the pressure contours on and around the vehicle are shown, and the aerodynamic forces and moments are presented in Table 2. Figure 20 is the convergence history of KSR-Ⅲ at the initial stage. Comparing these aerodynamic characteristics with those of H-Ⅱ and CZ-3C, some interesting features are found. One of these features is that the axial force coefficient Cx of KSR-Ⅲ is about four times that of H-Ⅱ and CZ-3C. But, as H-Ⅱ is about eight times larger than KSR-Ⅲ in volume and mass of boosters, much more slow vertical motion of booster may be expected in the separation stages of KSR-Ⅲ. Another significant feature is that the normal force Cz shows positive sign and pitching moment Cm is negative, which are similar to the results of CZ-3C. Thus the booster motion of KSR-Ⅲ in the separation stages may be also similar to that of CZ-3C and some jettisoning force and moment may be needed at the moving stage to prevent the collision between core rocket and booster.

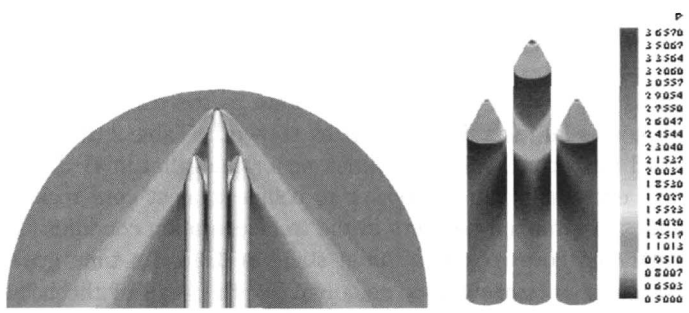

Fig. 19. Pressure contours of KSR-Ⅲ at the initial stage (Mach = 2.0, Re = 9.0047×10^6)
a) Around the Vehicle b) On the Surface of the Vehicle

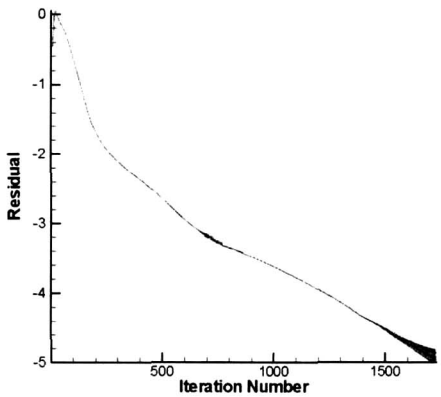

Fig. 20. Convergence History of KSR-III at the Initial Stage (Mach = 2.0, Re = 9.0047×10^6, CFL = 5.0)

These adverse aerodynamic features, which of course can not be found in H-II, seem to be from the interaction of shock or expansion waves between the core rocket and booster of KSR-III. Concerning these matters, some additional aerodynamic characteristics are examined at various attitudes of booster in order to analyze the effects of shock interaction between the core rocket and booster. As shown in Fig. 21, attitudes of booster are represented by two factors, the distance from the core rocket and the nose angle with respect to the core rocket. Firstly six cases of different separation distance are simulated: 0.15, 0.30, 0.45, 0.60, 0.75, 0.90 at 0 nose angle. In Fig. 22, pressure contours around the vehicles at different distances are shown. Secondly five cases of different nose angle are simulated: -4, -2, 0, +2, +4 at 0.60 separation distance. Pressure contours around the vehicles at different nose angles are shown in Fig. 23. In all cases the free stream Mach number, Reynolds number and grid sizes are the same as the previous. In Fig. 24-a, the aerodynamic forces and moments acting on the booster surface are shown at various distances. While the axial force Cx and the normal force Cz vary slowly, the nose up moment Cm is sensitive to separation distance. It is noted that the increase of separation distance may augment the negative trend of Cz. The behavior of Cm, on the other hand, changes from a negative to positive moment after 0.35 distance. Similarly in Fig. 24-b, the aerodynamic forces and moments are compared at various nose angles. Cx is almost constant in all cases, and Cz and Cm are increasing from negative to positive values according to the increment of the nose angle of the booster. The behavior of Cz and Cm is believed to be caused by the interaction of the shock and expansion waves between the core rocket and booster which directly affects the pressure distribution around the booster nose. These two results indicate that a suitable pair of jettisoning force and moment is necessary to guarantee a safe separation.

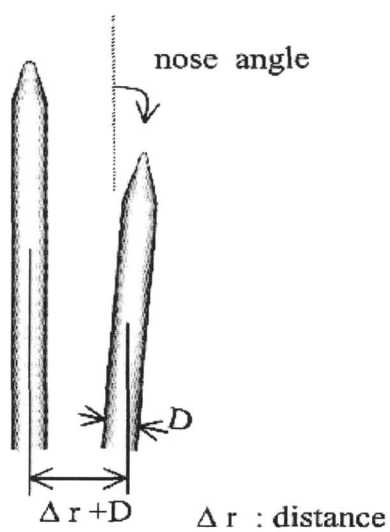

Fig. 21. Attitude definitions of booster

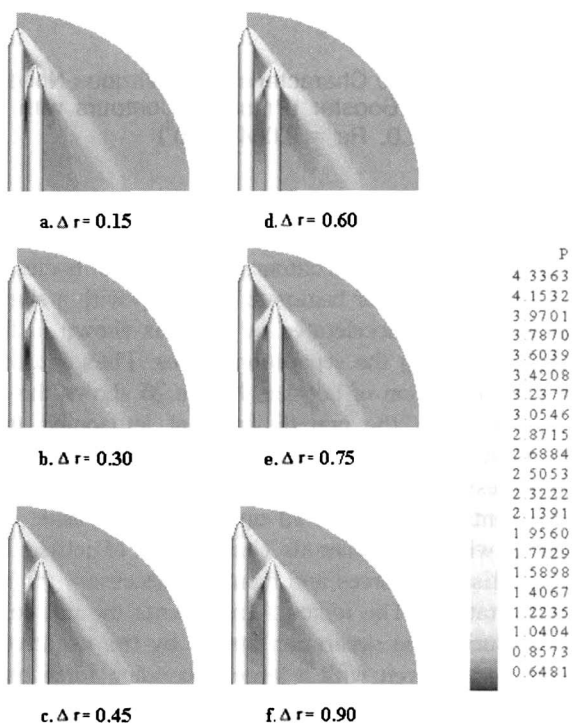

Fig. 22. Aerodynamic Characteristics at Various Distances of Booster (Pressure Contours with Mach = 2.0, Re = 9.0047×10^6)

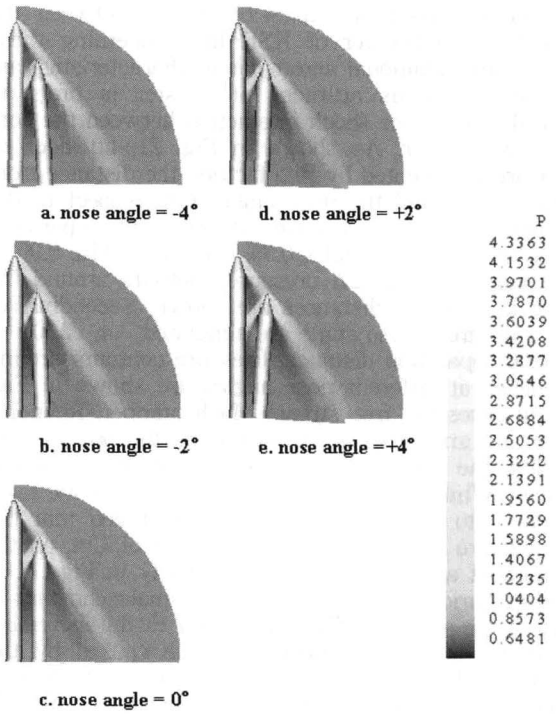

Fig. 23. Aerodynamic Characteristics at Various Nose Angles of Booster (Pressure Contours with Mach = 2.0, Re = 9.0047×10^6)

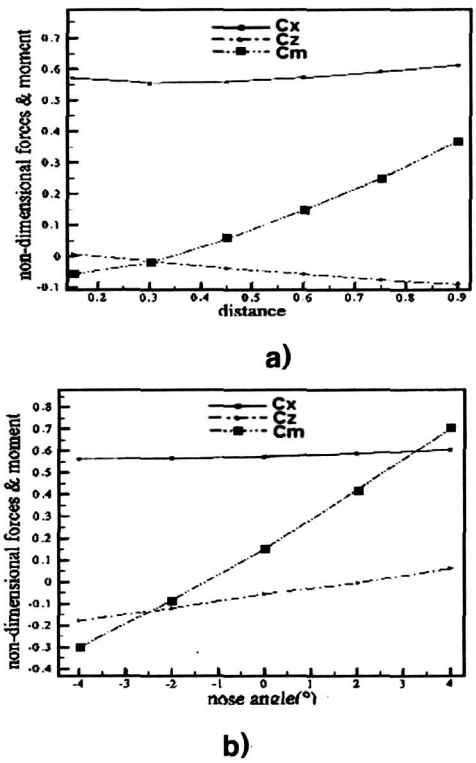

Fig. 24. Comparison of Aerodynamic Forces and Moments at Various Attitudes of Booster
a) Aerodynamic Forces and Moments at Various Distances
b) Aerodynamic Forces and Moments at Various Nose Angles

Then the separation dynamics of KSR-III is simulated at the physical time step of 0.005sec with the same free stream Mach number and Reynolds number. In Fig. 25, the trajectory of booster and corresponding pressure contours around the bodies are shown at every 0.1sec after free body separation. The booster begins to fall down with a slight negative pitching motion. Since this negative pitching motion is accelerated by itself as shown in the above attitude analyses, the upside collision is inevitable during the separation stages. Thus additional jettisoning forces and moments are needed for a safe separation of booster. Figure 26 shows the booster trajectory and pressure contour around the vehicle when the non-dimensional jettisoning moment of 0.356 acts on the booster. On the contrary, in this case the booster hits the downside of the core rocket after 0.4 sec of its separation due to excessive jettisoning moment. These results suggest that some restrictions of jettisoning forces and moments exists to avoid upside and downside collision. Then the forced separation cases are simulated with the numerous combination of jettisoning forces and moments. Figure 27 shows the map of jettisoning forces and moments necessary for the safe separation of the booster obtained from the computations. The region A represents the upside collision zone where the upside of booster hits the core during the separation stages by the negative aerodynamic pitching moment. In this region collision occurs even with a large jettisoning force because the jettisoning moment is not enough to overcome the negative pitching motion of booster. And the region B represents the downside collision zone where the excessive jettisoning moment causes too large positive pitching motion of the booster. Figure 28 shows an example of safe separation when the non-dimensional jettisoning force of 0.475 and moment of 0.238 act on the booster which is surely in the safe separation zone.

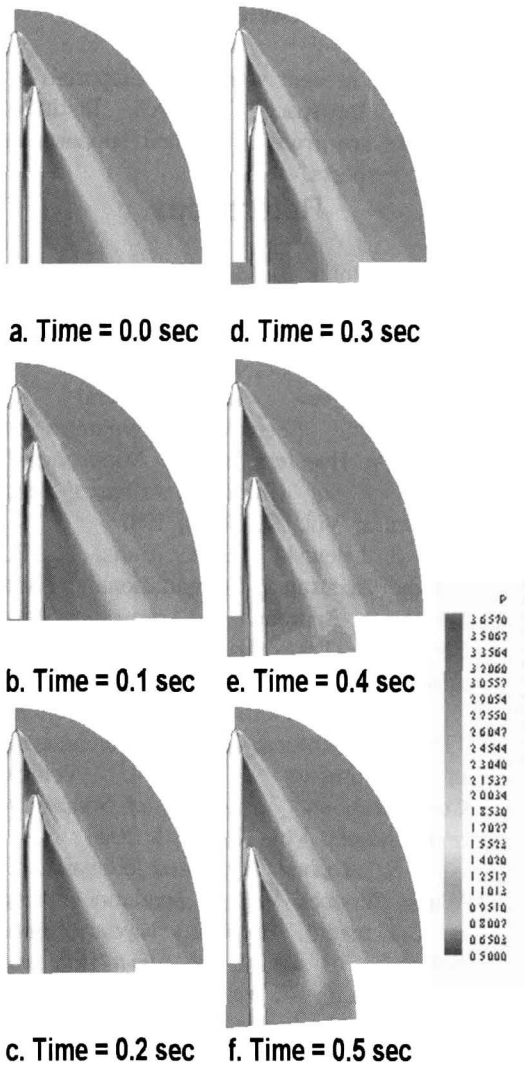

Fig. 25. Booster Trajectory of KSR-III with Pressure Contours (Free separation, no jettisoning force & moment)

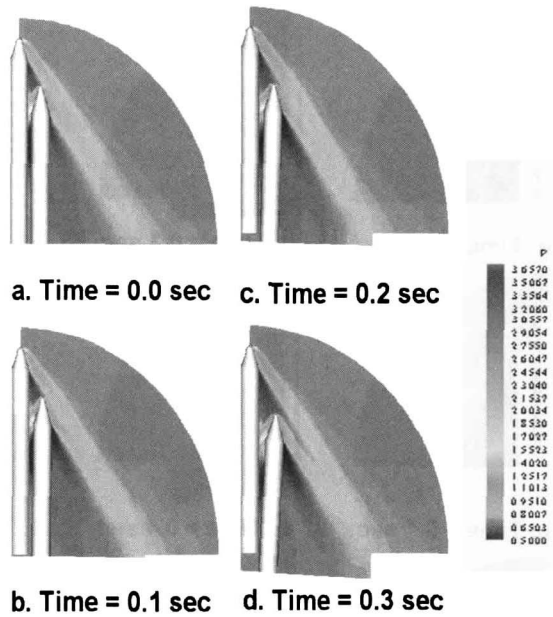

Fig. 26. Booster Trajectory of KSR-III with Pressure Contours (Non-dimensional jettisoning moment = 0.356)

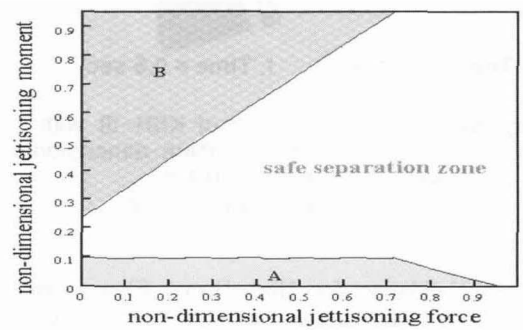

Fig. 27. Guideline Map of Jettisoning Force & Moment for KSR-III

Concluding Remarks

An efficient three-dimensional aerodynamic-dynamic coupled code with an overlapping moving grid scheme is developed in order to predict the trajectory of strap-on boosters separated in the dense atmosphere. A domain division technique is introduced for the grid scheme to reduce the computation time to find interpolation points. The trajectories of the separated boosters are then predicted for two types of vehicles. From the analyses, it is observed that the size of strap-ons may have significant effects on the separation dynamics. Vehicles with large strap-on boosters may accompany the interactions of shock or expansion waves between the core rocket and boosters and thus involve an upside or downside collision of bodies if the attitudes of boosters are not properly controlled. And in those collision cases, the guideline map of jettisoning force and moment guaranteeing the safe separation of boosters is presented.

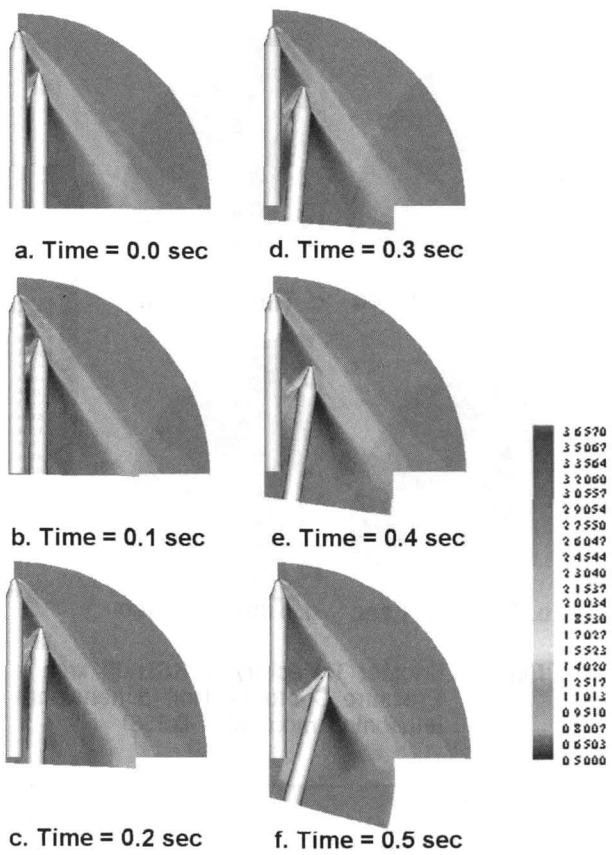

Fig. 28. Booster Trajectory of KSR-III with Pressure Contours (Non-dimensional jettisoning force = 0.475, jettisoning moment = 0.238)

Acknowledgement

The present work was supported by Korea Aerospace Research Institute. Authors are grateful for their supports in many respects.

References

1. Robert L. Meakin and Norman E. Suhs, "Unsteady Aerodynamic Simulation of Multiple Bodies in Relative Motion," *AIAA* 89-1996-CP, 1989

2. Rajeev Lochan and V. Adimurthy, "Separation Dynamics of Strap-On Boosters in the Atmosphere," *AIAA J. of Guidance, Control and Dynamics*, Vol. 20, No. 4, 1997

3. Lijewski, L. E., Suhs, N. E., "Time-Accurate Computational Fluid Dynamics Approach to Transonic Store Separation Trajectory Prediction," *J. of Aircraft*, Vol. 31, No. 4, 1994

4. Grant Palmer and Pieter Buning, "Three-Dimensional Computational Analysis of Complex launch Vehicle Configurations," *AIAA J. of Spacecraft and Rockets*, Vol. 33, No. 1, 1996

5. Stephen Taylor and Johnson C. T. Wang, "Launch-Vehicle Simulations Using a Concurrent, Implicit Navier-Stokes Solver," *AIAA J. of Spacecraft and Rockets*, Vol. 33, No. 5, 1996

6. J. L. Azevedo and P. Moraes Jr., "Code Validation for High-Speed Flow Simulation Over Satellite Launch Vehicle," *AIAA J. of Spacecraft and Rockets*, Vol. 33, No. 1, 1996

7. Baldwin, B. S., and Lomax, H., "Thin Layer Approximation and Algebraic Model for Separated Flow," *AIAA Paper* 78-257, Jan. 1978.

8. Degani, D., Schiff, L. B., "Computation of Turbulence Supersonic Flows Around Pointed Bodies Having Crossflow Separation," *Journal of Computational Physics*, Vol. 66, No. 1, 1986, pp. 173-196

9. Yoon, S., and Jameson, A., "Lower-Upper SymmetricGauss-Seidel Method for the Euler and Navier-Stokes Equations," *AIAA Journal*, Vol. 26, No. 9, 1988, pp. 1025-1026

10. Kyu Hong Kim, Chongam Kim and Oh Hyun Rho, "Accurate Computations of Hypersonic Flows Using AUSMPW+ Scheme and Shock-aligned-grid Technique," *AIAA Paper* 98-2442, 1998.

11. Van Leer, B., "Towards the Ultimate Conservative Difference Scheme. V. A Second Order Sequel to Godunovs Methods," *Journal of Computational Physics*, Vol. 32, 1979, pp.101-136

12. W. K. Anderson, J. L. Thomas, and B. Van Leer, "Comparison of Finite Volume Flux Vector Splittings for The Euler Equations," *AIAA Journal*, Vol. 24, No. 9, September, 1986, pp. 1453-1460

13. Steger, J.L., Dougherty, F.C. and Benek, J. A., "A Chimera Grid Scheme," *Advances in Grid Generation, FED* Vol.5, ASME, edited by Ghia. K. N., New Tork, 1983, pp. 59-69